【Review】 **DOI**: 10.13208/j.electrochem.210851 **Http**://electrochem.xmu.edu.cn

Recent Advances in Electrochemical Kinetics Simulations and Their Applications in Pt-based Fuel Cells

Ji-Li Li[1], Ye-Fei Li[1*], Zhi-Pan Liu[1,2*]

(*1. Collaborative Innovation Center of Chemistry for Energy Material, Key Laboratory of Computational Physical Science (Ministry of Education), Shanghai Key Laboratory of Molecular Catalysis and Innovative Materials, Department of Chemistry, Fudan University, Shanghai 200433, China; 2. Key Laboratory of Synthetic and Self-Assembly Chemistry for Organic Functional Molecules, Shanghai Institute of Organic Chemistry, Chinese Academy of Sciences, Shanghai 200032, China*)

Abstract: Theoretical simulations of electrocatalysis are vital for understanding the mechanism of the electrochemical process at the atomic level. It can help to reveal the *in-situ* structures of electrode surfaces and establish the microscopic mechanism of electrocatalysis, thereby solving the problems such as electrode oxidation and corrosion. However, there are still many problems in the theoretical electrochemical simulations, including the solvation effects, the electric double layer, and the structural transformation of electrodes. Here we review recent advances of theoretical methods in electrochemical modeling, in particular, the double reference approach, the periodic continuum solvation model based on the modified Poisson-Boltzmann equation (CM-MPB), and the stochastic surface walking method based on the machine learning potential energy surface (SSW-NN). The case studies of oxygen reduction reaction by using CM-MPB and SSW-NN are presented.

Key words: CM-MPB; machine learning; SSW; LASP

1 Introduction

The combustion of fossil fuels is the main source of greenhouse gas in the atmosphere, and is believed to be the major cause of global warming and climate change. To resolve this problem, great efforts have been devoted to developing fuel cells that can replace fossil fuels[1]. In this technology, the oxygen reduction reaction (ORR)[2,3] at the cathode is the bottleneck due to its sluggish kinetics. Among all candidates, Pt is the indispensable component of cathode due to its reasonable durability and reactivity[4,5]. However, high expense and high loading of Pt limit the large-scale application in industry[6]. To provide insight into the design of Pt-based electrocatalysts, an understanding of the active site and reaction mechanism for ORR is highly desirable[7-9].

Tafel slope is a key parameter of electrochemical kinetics from experiments, which connects the microscopical chemical reaction with the measurable *I-V* curve, and provides a feasible way to quantify the thermodynamics and kinetics of the reaction[10]. For ORR, the *I-V* curve exhibits two Tafel regions, one is below 0.8 V with a Tafel slope of ~ 120 mV, while the other is above 0.8 V with a Tafel slope of ~ 60 mV. The change of the Tafel slope indicates the rate-determining step (rds) in the mechanism alters at

Cite as: Li J L, Li Y F, Liu Z P. Recent advances in electrochemical kinetics simulations and their applications in Pt-based fuel cells. *J. Electrochem.*, 2022, 28(2): 2108511.

Received: 2021-11-04, Revised: 2021-12-21. *Corresponding author, Ye-Fei Li, E-mail: yefeil@fudan.edu.cn; Tel: (86)15216704663, Zhi-Pan Liu, Tel: (86-21)65642400, E-mail: zpliu@fudan.edu.cn

0.8 V. Importantly, this turning potential is just close to the working potential of Pt cathode in fuel cells. Revealing the physical origin of dissimilar electrochemical kinetics at different potentials may help to design a more efficient ORR electrocatalyst.

The electric double layer, an interphase region at the electrode/electrolyte interface, is essential in electrocatalysis, and plays a key role in electrochemical kinetics. In the electric double layer, the distribution and oriented arrangement of ions are biased, which generates residual charges and causes a strong electric field around the electrode surface. The electric double layer can be described by the Gouy-Chapman-Stern model[11-13], as shown in Figure 1(A). The layer closest to the electrode, the compact layer, contains solvent molecules and some other species that are adsorbed specially on the electrode. The non-specifically adsorbed ions are distributed in a three-dimensional region called the diffuse layer, which extends from the compact layer into the bulk of the solution. Although the concept of electric double layer has been proposed for more than one hundred years, its detailed structure and influence on electrocatalysis are still far from clear.

The surface structures of Pt electrocatalysts would be notably changed during ORR, which may also affect the ORR activity. By applying the repeated square-wave potentials at -0.2 V and +1.20 V vs. SCE, Tian et al. reported that a series of high-index faces with a high density of surface steps and open (100) terraces dominate on the Pt electrode surface. This result implies that the close-packed Pt(111) is not always the most stable surface under electrochemical treatment[4,14].

With the rapid development of the theoretical methods in recent years, researchers have been able to simulate the electrochemical kinetics that concerns the solid structure, solvents, and electrolyte species at the charged electrode/electrolyte (solid/liquid) interface[15]. For instance, a periodic continuum solvation model based on the modified Poisson-Boltzmann equation (CM-MPB)[16-18] has been proposed, which accounts for the electric double layer, the short-range and long-range solvent effects at the electrode/electrolyte interface. To track the *in-situ* atomic structural evolution under electrochemical conditions, several novel global potential energy surface (PES) search methods, such as the stochastic surface walking (SSW)[19,20], genetic algorithm[21], and basin-hopping[22] have been applied. To speed up the calculations, machine learning (ML) has been utilized to construct the PES and to perform property predictions based on the density functional theory (DFT) or experimental data[23].

In this review, we focus on the recent theoretical advances in ORR simulations of Pt-based electrocatalysts. We first introduce the computational methods and models developed for electrochemistry. Then, we discuss the application of CM-MPB combined with DFT (DFT/CM-MPB) to explore electrochemical kinetics. At last, we present our recently developed SSW-NN in exploring the structural evolution of the Pt-based catalysts under working conditions.

2 Computational Methods for Electrocatalysis

2.1 Computational Hydrogen Electrode Method

The computational hydrogen electrode (CHE) method is the most widely used approach to evaluate the thermodynamics of elemental steps in electrocatalysis[24]. The key is to relate the electrochemical potentials of solvated protons and electrons with the gaseous H_2 under standard conditions:

$$\mu(\mathrm{H^+}) + \mu(\mathrm{e^-}) = \frac{1}{2}\mu(\mathrm{H_2}) - eU \tag{2.1}$$

where U is the electrode potential. With this relationship, the free energy change of each electrochemical step can be obtained by standard DFT calculations of each intermediate species:

$$\Delta G = \Delta E + \Delta E_{\mathrm{ZPE}} - T\Delta S + \int C_p \,\mathrm{d}T \tag{2.2}$$

where is the energy difference directly from DFT calculations; ΔE_{ZPE}, $T\Delta S$, and $\int C_p \,\mathrm{d}T$ are zero-point energy (ZPE), entropy, and enthalpy corrections, respectively. For adsorbed species, thermal corrections largely come from the vibration, and can be calculated by the vibration frequencies v_i, as shown in Eqs.

(2.3)-(2.5)

$$\Delta E_{\mathrm{ZPE}} = \frac{1}{2}\sum_i h\nu_i \tag{2.3}$$

$$-\Delta S = k_B T \sum_i \ln\left(1 - e^{-\frac{h\nu_i}{k_B T}}\right) - \sum_i h\nu_i \left(\frac{1}{e^{\frac{h\nu_i}{k_B T}} - 1}\right) \tag{2.4}$$

$$\int C_p \,\mathrm{d}T = \sum_i h\nu_i \left(\frac{1}{e^{\frac{h\nu_i}{k_B T}} - 1}\right) \tag{2.5}$$

While for free molecules in gas and liquid phases, the contributions from translation and rotation could be further included.

2.2 Simulations of the Electric Double Layer

There are two approaches to deal with the electric double layer. The one is the constant electron chemical potential mode, while the other one is the constant electron number mode. In the constant electron chemical potential mode, a grand canonical approach is implemented within the DFT framework, which allows the variety of electron number during the simulations. The constant electron chemical potential mode is first developed by Lozovoi et al.[25], in which a reference electrode is introduced into the supercell to neutralize the charge, and carried by the slab metal. As for the constant electron number mode, the electron number is fixed during simulations. The constant electron number mode can be easily carried out with the standard DFT code, so it is widely used in the literature[26]. In the following, we will introduce two popular methods in the constant electron number mode, namely, (i) double reference approach and (ii) Periodic Continuum Solvation Model based on the Modified Poisson-Boltzmann Equation (CM-MPB).

2.2.1 Double Reference Approach

The double reference approach, as proposed by Neurock's group[27], simulates the electric double layer by adding/removing a predetermined number of electrons to/from a periodic metal slab. A homogeneous compensating charge is added to maintain overall charge neutrality. Then, a full water layer is introduced over the vacuum region between the metal slabs to explicitly model the solvent effect, as shown in Figure 1(B). The charged slab along with the homogeneous compensating charging polarizes the water layers thus simulating the electric double layer. The resulting electrode potential is compared to an internal reference potential, the vacuum level, by artificially inserting a very thin vacuum layer into the center of the water layers. All other potentials can then be shifted accordingly and referenced to the vacuum level. The following expression (Eq. 2.6) is then used to compare the results from the vacuum to the standard hydrogen electrode (SHE).

$$\phi_{\mathrm{SHE}} = -4.85\ \mathrm{eV} - \phi_{\mathrm{vac}} \tag{2.6}$$

where 4.85 eV is the absolute position of SHE relative to the vacuum level. Note that the value is not well determined and is commonly taken from experiments ranging from 4.44 eV to 4.85 eV[28]. The electrode potential (U) is related to the work function of

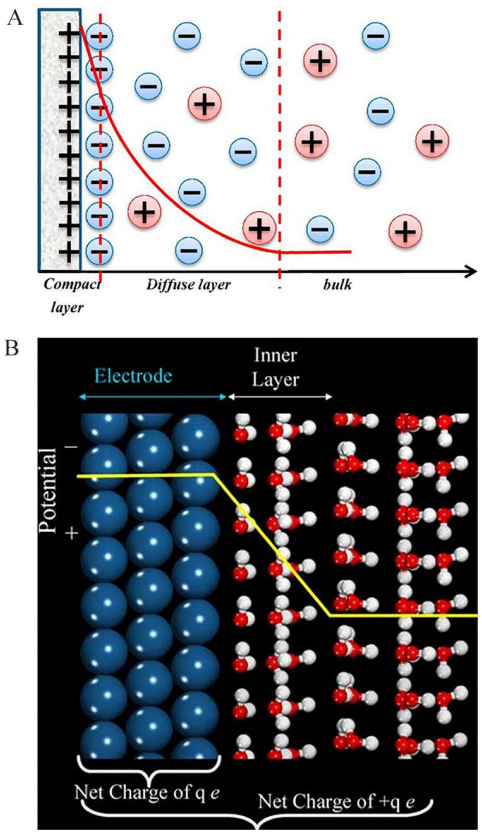

Figure 1. (A) Gouy-Chapman-Stern representation of electric double layer[10]. (B) The periodic slab employed with the double-reference method to determine the potential[29]. Reproduced with permission of Ref. 10 (A) and Ref. 29 (B). Copyright with 2014 American Chemical Society and Copyright with 2007 Springer Science Business Media, LLC. (color on line)

the system and the SHE:

$$U = \phi - \phi_{SHE} \tag{2.7}$$

The work function ϕ is defined by the potential of the electrons (at the Fermi level) relative to a vacuum, E_{vac} - E_{fermi}, and it changes with the varying of the electrons.

2.2.2 CM-MPB

The CM-MPB uses the charged metal slab to simulate the electric double layer, similar to the double reference approach. The compensating charge, however, is distributed following the modified Poisson-Boltzmann equation at the grid points of vacuum region in the periodic slab calculations, as shown in Eq. (2.8)

$$\rho_{\pm}(r) = \mp \frac{c_b e[\pm\phi(r) - \phi_{rep}/k_B T]}{1 - v + v\cosh[\phi(r)/k_B T]e^{-\phi_{rep}/k_B T}} \tag{2.8}$$

$\rho_{\pm}(r)$is the electron density distribution of anion and cation; $\phi(r)$ is the electrostatic potential; $v = 2a^3c_b$, a parameter relating to electrolyte, a is the effective ion size and c_b is the bulk concentration of the electrolyte. The solvent molecules are treated implicitly by the periodic continuum solvent model, which is firstly proposed by Fattebert and Gygi[30,31] The critical quantity in the periodic continuum solvation model equation is the smooth dielectric function $\varepsilon(r)$ at the solid-liquid interface, as shown in Eq. (2.9):

$$\varepsilon\rho(r)) = 1 + \frac{\varepsilon_\infty - 1}{2}\left(1 + \frac{1-\left(\frac{\rho(r)}{\rho_0}\right)2\beta}{1+\left(\frac{\rho(r)}{\rho_0}\right)2\beta}\right) \tag{2.9}$$

ε_∞ is the dielectric function of bulk electrolyte. becomes ε_∞ when the electron density approaches 0, while it becomes 1 when the electron density is high. ρ_0 is the threshold of electron density $\rho(r)$ to adjust the size of the cavity. β determines the smoothness of the transition from 1 to ε_∞. ρ_0 and β are chosen by fitting the experimental solvation energy. For aqueous solutions, ρ_0 and β are 0.00078 e·Bohr^{-3} and 1.3, respectively. By substituting Eqs. (2.8) and (2.9) into the Poisson equation, the electrostatic potential is resolved, as shown in Eq.(2.10)

$$\nabla\cdot(\varepsilon(\rho(r))\nabla(\phi)) = -4\pi\rho + 8\pi z e c_b \frac{\sinh\left(\frac{ze\phi}{kT}\right)}{1 - v + v\cosh\left(\frac{ze\phi}{kT}\right)} \tag{2.10}$$

The contribution of the ions in the electric double layer is determined by the second term in the right-hand side of Eq. (2.10), which can be solved iteratively during electronic structure loops. The vacuum level is the potential at the middle of vacuum region, and the electrode potential is calculated by Eqs. (2.6)-(2.7). Finally, the electrostatic potential energy, E_{es}, can then be calculated by

$$E_{es} = \int dr[\rho_e(r) + \rho_c(r) + \rho_-(r) + \rho_+(r)]\phi(r) - \int dr\frac{\varepsilon(r)}{8\pi}|\nabla\phi(r)|^2 \tag{2.11}$$

Liu's group has implemented the CM-MPB into the standard periodic DFT code, SIESTA[32,33], and

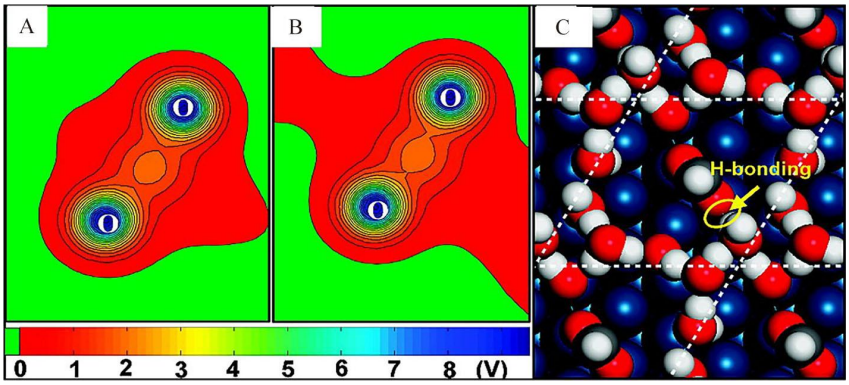

Figure 2. Contour plots of total electrostatic potential for formate-adsorbed Pt(111) (A) without and (B) with the continuum solvation shell; (C) MD snapshot for the formate-adsorbed Pt(111)/H_2O system taken after 10 ps NVT simulation at 300 K[16]. Reproduced with permission of Ref 16. Copyright with 2009 American Chemical Society. (color on line)

performed benchmarks on the formate-adsorbed Pt (111) surface. Figure 2 shows the electrostatic potentials with and without the CM-MPB model. The results show that the subsequent solvation by the dielectric leads to the further accumulation of electrons in the region, where the positive potential region was significantly enlarged in area with the continuum solvation model. This feature is confirmed by the molecular dynamics (MD) snapshot of the formate-adsorbed Pt/H_2O interface, which shows a hydrophobic hole around the formate.

2.3 Tafel Kinetics from First-Principles Calculations

Tafel slope is directly related to the electrochemical kinetics, and thereby, a convenient way to analyze the reaction mechanism. Tafel slope is expressed by the Tafel equation.

$$\eta = a + b\lg i \tag{2.12}$$

$$b = \frac{2.303RT}{\alpha F} \tag{2.13}$$

where b is the Tafel slop; η is the overpotential; is the charge transfer coefficient (CTC). The CTC is an important quantity in electrochemistry because it connects the measurable Tafel slope with the microcosmic reaction mechanism. For example, if the rds involves one-electron transfer with the CTC of 0.5, the overall reaction has the Tafel slopes of $RT/(n+0.5)F$, where n is the number of electron transfer before rds (n = 0, $2RT/F$ ~ 120 mV at 298 K; n =1, $2RT/3F$ ~ 40 mV). On the other hand, if the rds involves zero electron transfer with the CTC of 0, the overall reaction has the Tafel slopes of RT/nF (n = 1, RT/F ~ 60 mV; n = 2, $RT/2F$ ~ 30 mV). The CTC is given by Eq. (2.14).

$$\alpha = \frac{\partial \Delta G_\alpha}{F \Delta U} \tag{2.14}$$

where ΔG_α is the free energy barrier and U is the electrode potential. Both terms can be calculated by the CM-MPB method. The current density jtot can be calculated by summing the contributions j_p from all the possible reaction pathways, as shown in Eqs. (2.15)-(2.17).

$$j = \sum_i j_i = \sum_i (j_{o,i} - j_{R,i}) \tag{2.15}$$

$$j_{o,i/R,i} = AFS^{-1}N_A^{-1}e^{-\Delta G_\alpha(U)/RT}[R] \tag{2.16}$$

$$\Delta G_\alpha(U) = -RT\ln[\sum_i x_i(U)e^{-\Delta G_\alpha(\theta_i,U)/RT}] \tag{2.17}$$

j_o is the current of oxidation and j_R is the current of the reduction; ΔG_α is the apparent free energy barrier; x_i is the relative portion of a phase; θ_i is the phase surface coverage; $\Delta G_\alpha(\theta_i, U)$ is the free energy barrier in each reaction pathway; A is the pre-exponential factor; S is the total surface area; $[R]$ is the concentration of surface sites.

2.4 SS W-NN Global Optimization and LASP Package

In 2013, Liu's group proposed the SSW global optimization method for molecules and clusters, which is later extended to periodic crystals[19,34]. The SSW method has become a powerful tool to reveal the structural evolution of catalysts under working conditions, including electrocatalysis[35], photocatalysis[17,36], and thermocatalysis[37]. As shown in Figure 3(A), an automated climbing mechanism is implemented to manipulate a structural configuration moving smoothly from the local minima to a high-energy configuration along one random mode direction. Each SSW step contains three independent parts, namely, climbing up the hill along PES, optimization, and Metropolis MC selection whether to accept or not.

In order to speed up the global PES search, the state-of-the-art machine learning technique has been applied. The key point is to parameterize the atomic interaction energy into the neural network as a function of the structure descriptor constructed locally by the component species. Behler et al. proposed a high-dimensional neural network (NN) potential (see Figure 3(B))[38], which splits the total energy as the summation of individual atomic energy:

$$E = \sum_i E_i \tag{2.18}$$

where E_i for each atom is the output of a standard feed-forward neural network (NN). The input of NN potential is a set of structural descriptors to describe the atom bonding environment. The NN parameters can be trained using the first-principles potential energy surface (PES) data set. Liu et al. proposed that, due to the smoothness of the SSW trajectory, the structures can be used to build the NN PES (SSW-NN)[39,40].

Furthermore, the input layer of NN utilizes sophisticated power-type structure descriptors (PTSDs), which can well describe the geometrical environment of atom and is compatible with the SSW trajectory. In SSW-NN, there are six types of PTSDs (S1-S6) that have the following mathematic forms:

$$f_c(R_{ij}) = \begin{cases} 0.5 \times \tanh^3\left[1-\frac{r_{ij}}{r_c}\right], & \text{for } r_{ij} \leqslant r_c \\ 0, & \text{for } r_{ij} > r_c \end{cases} \quad (2.19)$$

$$R^n(r_{ij}) = r_{ij}^n \cdot f_c(r_{ij}) \quad (2.20)$$

$$S_i^1 = \sum_{j\neq i} R^n(r_{ij}) \quad (2.21)$$

$$S_i^2 = \left[\sum_{m=-L}^{L} |\sum GU_2|^2\right]^{\frac{1}{2}} = \left[\sum_{m=-L}^{L} \left|\sum_{j\neq i} R^n(r_{ij}) Y_{Lm}(r_{ij})\right|^2\right]^{\frac{1}{2}} \quad (2.22)$$

$$S_i^3 = 2^{1-\zeta}\sum GU_3 = 2^{1-\zeta}\sum_{j,k\neq i}(1+\lambda\cos\theta_{ijk})^{\zeta} \cdot R^n(r_{ij}) \cdot R^m(r_{ik}) \quad (2.23)$$

$$S_i^4 = 2^{1-\zeta}\sum GU_4 = 2^{1-\zeta}\sum_{j,k\neq i}(1+\lambda\cos\theta_{ijk})^{\zeta} \cdot R^n(r_{ij}) \cdot R^m(r_{ik}) \cdot R^p(r_{ik}) \quad (2.24)$$

$$S_i^5 = \left[\sum_{m=-L}^{L} |\sum GU_5|^2\right]^{\frac{1}{2}} = \left[\sum_{m=-L}^{L} \left|\sum_{j,k\neq i} R^n(r_{ij}) \cdot R^m(r_{ik}) \cdot R^p(r_{ik}) \cdot (YL_m(r_{ij}) + YL_m(r_{ik}))\right|^2\right]^{\frac{1}{2}} \quad (2.25)$$

$$S_i^6 = 2^{1-\zeta}\sum GU_6 = 2^{1-\zeta}\sum_{j,k,l\neq i}(1+\lambda\cos\theta_{ijk})^{\zeta} \cdot R^n(r_{ij}) \cdot R^m(r_{ik}) \cdot R^p(r_{ik}) \quad (2.26)$$

The application of SSW-NN method can be divided into six steps (see Figure 3 (C)): (1) Generating the global dataset from the SSW global optimization trajectories and computing the dataset using DFT calculation; (2) Training the NN potential with dataset; (3) Benchmarking the accuracy between the current NN potential and DFT calculation for selected structures from SSW trajectories and retraining the NN potential by adding new dataset; (4) Iteratively performing (1-3) steps until the PES deviation is low enough. The accuracy for G-NN potential is typically 5 ~ 10 meV·atom^{-1} for RMSE of energy and 0.1 ~ 0.2 eV·Å^{-1} for RMSE of force; (5) Performing the SSW global optimization on the NN PES for target problem. (6) Recomputing the energy of key structures with DFT calculations, in which Bayesian optimization is utilized to drive the iterative acquisition-surrogate procedure.

The SSW-NN method is implemented in the LASP software developed by Liu's group[40]. The initial objective of LASP is to merge two major simulation tools, SSW global optimization and NN PES, into a single package for better and simpler usage. LASP is now shaped toward a software platform for many

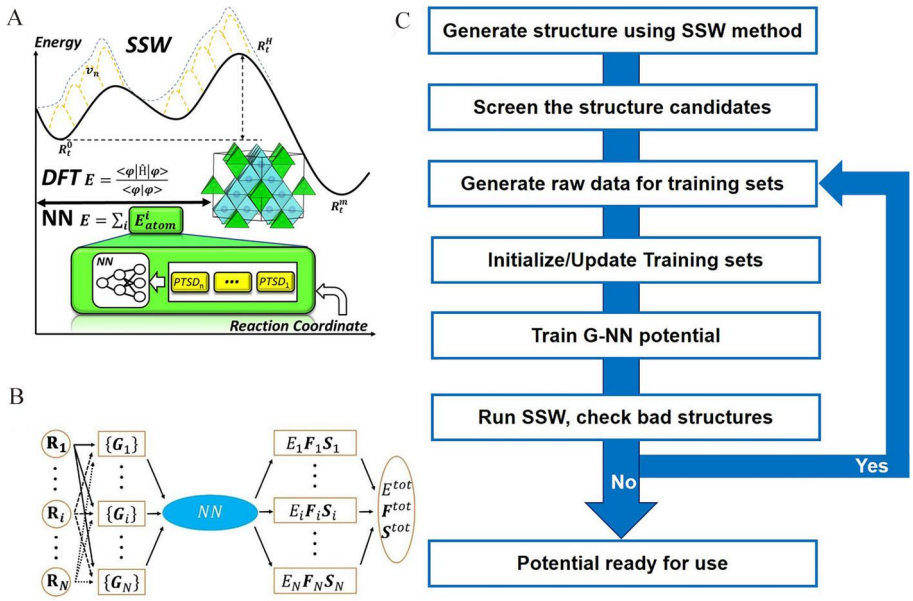

Figure 3. (A) Illustration of the SSW global optimization. (B) Scheme for the Behlar NN architecture[39]. (C) Procedure for generating the training dataset using SSW global optimization. Reproduced with permission of Ref. 39 (B). Copyright with 2017 Royal Society of Chemistry. (color on line)

purposes, not only for atomistic simulation, but also for PES data building and exchange, and even for global NN potential generation. A large set of powerful simulation techniques has been assembled into LASP program (www.lasphub.com) to simplify the usage and to enlarge the scope of the current atomistic simulation.

3 ORR on Pt-Based Electrocatalysts

3.1 Tafel Kinetics of ORR on Pristine Pt (111) by CM-MPB Method

Tafel slope is the key parameter of electrochemical kinetics. As the first step of Tafel kinetics simulations, the surface Pourbaix diagram of adsorbates, i.e., the *in-situ* coverages for *O, *OH, should be examined, because they can significantly affect the kinetics of ORR. However, the mixed phase of *OH + *O is difficult to be handled because of their numerous configurations. Various studies found that the stabilities of the mixed phase of *OH + *O are generally close to that of one specific O phase[32,41]. For instance, Fang et al. pointed out that the stabilities of 0.75 ML of O and 0.75 ML of O + 0.00625 ML of OH are nearly

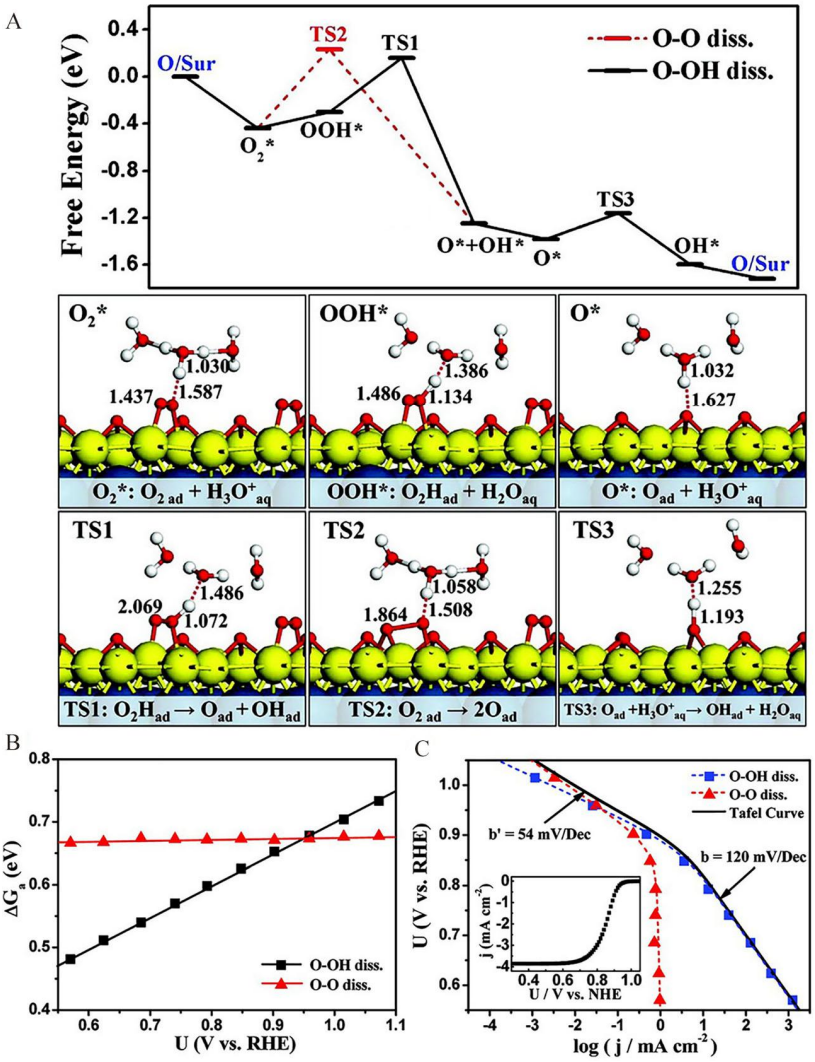

Figure 4. (A) Free energy profiles for ORR on Pt (111) at 0.8 V and the structural snapshots of *O_2, *OOH, *O, TS1, TS2, and TS3. (B) Plots for the free energy barrier (ΔG_a) vs. potential (U) of two reaction pathways for ORR on Pt(111). (C) Tafel curve and the contributions from two reaction pathways. The insert in (C) is the *I-V* curve with the maximum limiting current at the low potentials being ~ -3.9 mA·cm^{-2} as determined from experiment[42]. Reproduced with permission of Ref 42 (A) and Ref 42 (B-C). Copyright with 2012 American Chemical Society and Copyright with 2012 American Chemical Society. (color on line)

identical[32]. Therefore, many studies use the pure O adsorbed situations to dictate the surface phase diagram of Pt.

Wei et al., for the first time, calculated the Tafel slope of ORR on Pt(111) by using DFT combined with CM-MPB (DFT/CM-MPB)[42]. They first evaluated the phase diagram of Pt(111), and showed that the surface is covered by 0.25 ML *O at 0.8 V vs. RHE. On this surface, they identified two reaction pathways, namely, O-OH dissociation and O-O dissociation paths, which have comparable barrier (ΔG_a) values of 0.60 eV and 0.67 eV, respectively, as shown in Figure 4(A).

O-OH (dissociation) path:

$$* + O_2 \rightarrow *O_2 \quad (3.1)$$

$$*O_2 + H^+ + e^- \rightarrow *OOH \quad (3.2)$$

$$*OOH \rightarrow *O + *OH \quad (3.3)$$

$$*O + *OH + 3(H^+ + e^-) \rightarrow 2H_2O_{(l)} + * \quad (3.4)$$

O-O (dissociation) path:

$$* + O_2(g) \rightarrow *O_2 \quad (3.5)$$

$$*O_2 \rightarrow 2*O \quad (3.6)$$

$$2*O + 4(H^+ + e^-) \rightarrow 2H_2O_{(l)} + * \quad (3.7)$$

In both pathways, the $*O_2$ state is the resting state, while the TS1 and TS2 determine the overall barriers of O-OH and O-O dissociation pathways. In the TS1 state, a proton transfers from the nearby H_3O^+ to the $*O_2$, indicating that the rds of O-OH dissociation pathway is a proton-coupled electron transfer (PCET) step. In contrast, the proton transfer does not occur at the TS2 state, suggesting that the proton transfer and electron transfer are decoupled at the O-O dissociation pathway. Consistently, the diagram of ΔG_a vs. U (see Figure 4(B)) shows that the barrier of O-OH dissociation pathway decreases linearly with the increase of potential U, while the barrier of O-O dissociation pathway is rather constant over the potential range investigated. This difference leads to the distinct CTC, that is 0.50 and 0 for O-OH and O-O dissociation pathways, respectively.

According to the Tafel equation, the *I-V* curve and the contributions from the two pathways are calculated, as shown in Figure 4(C). The *I-V* curve exhibits two linear regions that switch at 0.85 V, with Tafel slopes of 120 mV and 54 mV. The current in the low potential region is dominantly contributed from the OOH dissociation pathway due to its low intrinsic barrier. While in the high potential region, the current largely arises from the O-O dissociation pathway, due to its higher CTC and thereby faster decrease of barrier compared to the O-OH dissociation pathway. This result can well explain the *I-V* curve in experiments[43], and demonstrates that the DFT/CM-MPB method can capture the physical origin of electrochemical kinetics.

3.2 The Corrosions of Pt and Pt_2M Alloys under ORR Conditions

3.2.1 Pure Pt

At high electrode potentials (U > 1.05 V), the Pt electrode surface is corroded due to the presence of high-coverage O atoms. To clarify the corrosion mechanism, Fang et al. investigated the thermodynamics of O generation and Pt leaching on Pt(111), Pt(211), and (100) faces. The results demonstrated that the corrosion of Pt electrode occurs via three steps[44], as shown in Figure 5(A):

Step I:

$$xH_2O + Pt_s \rightarrow O_x/Pt_s + 2xH^+(aq) + 2xe^- \quad (3.8)$$

Step II:

$$O_x/Pt_s \rightarrow O_{x-y}\text{-}PtO_y/Pt_s \quad (3.9)$$

Step III:

$$O_{x-y}/PtO_y/Pt_s \rightarrow O_{x-y-\square}/Pt_s + Pt^{2+} + 2e^- \quad (3.10)$$

where O_x/Pts and $O_{x-y}/PtO_y/Pt_s$ are the Pt surfaces without and with subsurface O, respectively; □ is the Pt vacancy. In the first step, the O coverage progressively increases up to 0.625 ML, 0.67 ML, and 1 ML O on Pt(111), (211), and (100), respectively, evident from the zero quasi-differential oxygen adsorption energy (see Figure 5(A) and 5(B)). In the second step, some O atoms penetrate into the subsurface of Pt electrode (see the green cycles in the phase-II of Figure 5(E)). In the third step, some Pt atoms that bond with subsurface O dissolve into the solution, leaving surface vacancies on the electrode.

By evaluating the free energy changes of three steps, Eqs. (3.8)-(3.10), Fang et al. showed that the penetration of O atoms and the dissolution of Pt

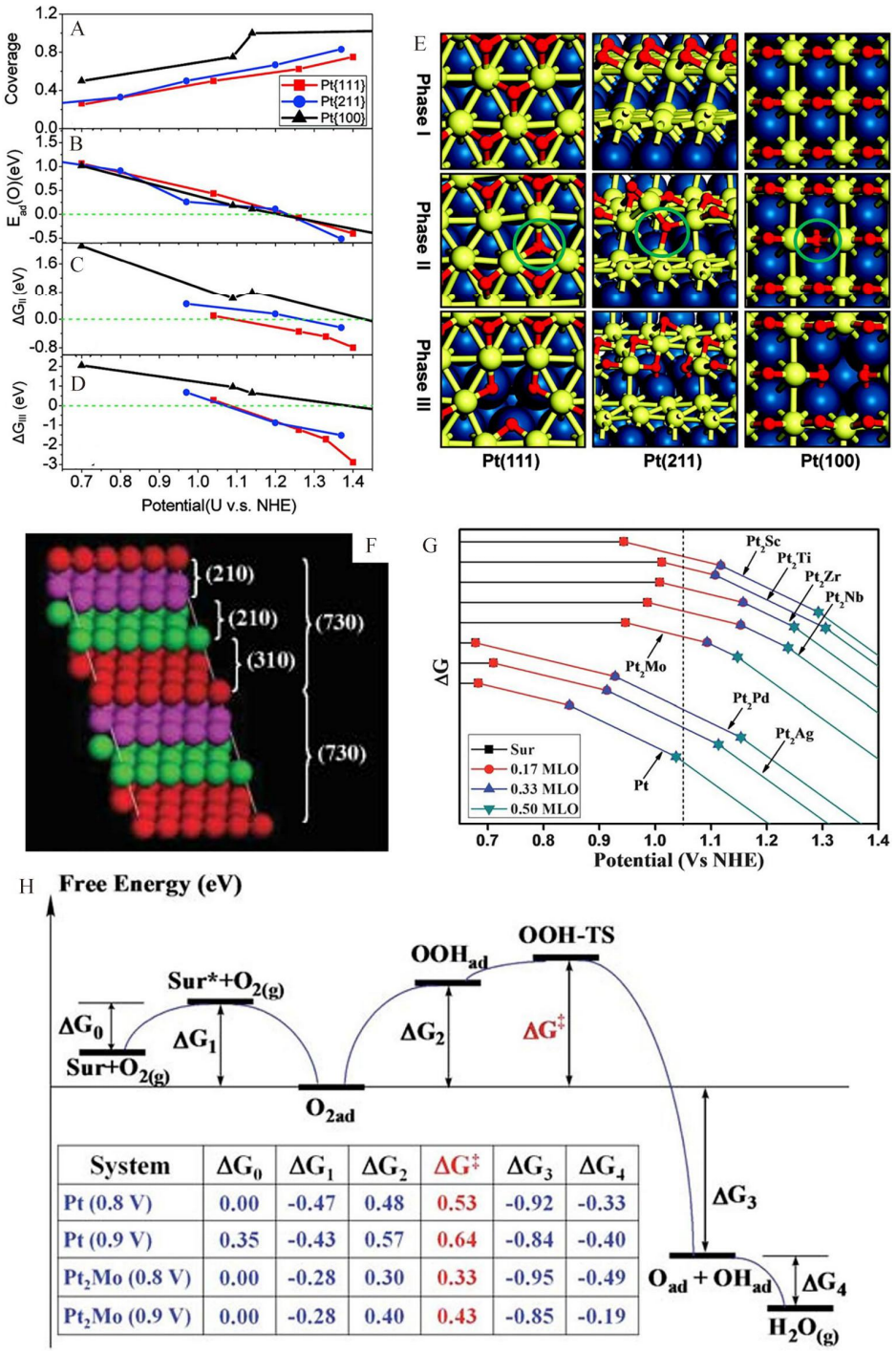

System	ΔG_0	ΔG_1	ΔG_2	$\Delta G^{\ddagger}$	ΔG_3	ΔG_4
Pt (0.8 V)	0.00	-0.47	0.48	0.53	-0.92	-0.33
Pt (0.9 V)	0.35	-0.43	0.57	0.64	-0.84	-0.40
Pt_2Mo (0.8 V)	0.00	-0.28	0.30	0.33	-0.95	-0.49
Pt_2Mo (0.9 V)	0.00	-0.28	0.40	0.43	-0.85	-0.19

Figure 5. Free energy diagram and the stable structures for each stage. (A) The O coverage; (B) The quasidifferential oxygen adsorption energy[44]; (C-D) Formation free energy of the phase-II (ΔG_{II}) and the phase-III (ΔG_{II}) as described in Reactions (3.9) and (3.10)[44]; (E) Structures for the surface adsorption phase (the phase-I), subsurface O phase (the phase-II), and surface vacancy phase (the phase-III) for the 0.625 ML O, 0.67 ML O and 1 ML O covered Pt(111), Pt(211), and Pt(100) surfaces at 1.2 V, respectively. Blue balls: subsurface Pt; yellow balls: surface Pt; red balls: O[44]. (F) Atomic model of Pt(730) plane with a high density of stepped surface atoms[4]. (G) Surface phase diagram of Pt(111) and Pt_2M (M = Sc, Ti, Zr, Nb, Mo, Pd, Ag) alloys[45]. (H) Schematic free energy profile for the O-OH dissociation pathway for ORR on Pt(111) and Pt_2Mo(111)[45]. Reproduced with permission of Ref. 44 (A-E), Ref. 4 (F), Ref. 45 (G) and Ref. 45 (H). Copyright with 2010 American Chemical Society, Copyright with 2007 The American Association for the Advancement of Science,Copyright with 2011 Royal Society of Chemistry and Copyright with 2011 Royal Society of Chemistry. (color on line)

atoms are thermodynamically favorable on Pt(111) at $U > 1.1$ V (see Figure 5(C) and 5(D)), indicating that the surface is unstable at high potentials. On the other hand, the Pt(100) and (211) faces are still stable at the same condition. Altogether, they suggested that the open Pt(100) and stepped (211) can resist the corrosion, while the close-packed Pt(111) cannot. This finding is consistent with Tian et al.'s report from experiments, which showed that only the high-index faces, such as (730), (520), (310), and (210), survive on the Pt electrode surface after applying a square-wave potential between -0.2 V and +1.20 V vs. SCE[4]. These high-index faces consist of {100} terraces and {n10} steps, as shown in Figure 5(F).

3.2.2 Pt_2M alloy

Pt alloys can reduce the cost of ORR electrocatalysts, and regulate their durability and activity. To screen the promising candidate for Pt alloy, Wei et al. screened all Pt_2M alloys (M = 3d and 4d metals) by examining the potential-dependent O coverage, energetics of Pt dissolution, and ORR barrier[45]. Figure 5(G) shows that Pt_2Ti, Pt_2Zr, Pt_2Mo, Pt_2Nb, and Pt_2Sc alloys have the lowest O coverage of 0.17 ML at 1.05 V, followed by Pt_2Pd and Pt_2Ag with 0.33 ML *O coverage (c.f., 0.5 ML *O on pure Pt). Accordingly, the free energy changes of the Pt dissolution on these O covered alloy surfaces are found to be -0.25 (Pt_2Sc), -0.21 (Pt_2Ti), -0.48 (Pt_2Zr), -0.15 (Pt_2Nb), 0.22 (Pt_2Mo), -0.07 (Pt_2Ag) and -0.08 eV (Pt_2Pd). As a result, Pt_2Mo exhibits higher stability than pure Pt among all candidates. Based on the high stability of Pt_2Mo, Wei et al. calculated the free energy profile for ORR on Pt_2Mo (111) and compared it with that on Pt(111), as shown in Figure 5H. At 0.9 V, the overall barrier on Pt_2Mo is 0.43 eV, which is 0.2 eV lower than that on pure Pt. The difference in barrier can lead to a three-order increase of rate according to microkinetics.

3.3 Size and Shape Effects on the ORR Activity

Besides the face and composition, the morphology (size and shape) of Pt nanoparticles is another important issue for ORR. Wei et al. investigated the shapes and ORR activities of Pt nanoparticles with diameters of 1 ~ 6 nm by using DFT calculations. Figure 6(A) illustrates the size-dependent equilibrium shapes of Pt nanoparticles by an improved Wulff construction that accounts for the energies from surfaces, edges, and corners[46]. The results show that the shape of bare Pt nanoparticles is a truncated octahedron that consists of eight {111} and six {100} faces. As the particle size increases, the Pt nanoparticles approach the cuboctahedron with the smaller $D_{(100)}/D_{(111)}$ ratio ($D_{(100)}$ and $D_{(111)}$ are the particle sizes along the <100> and <111> directions, respectively). The trend of morphology for Pt nanoparticles is well consistent with that observed in experiments[47].

Under ORR conditions, the surface of Pt nanoparticles may be covered by O atoms. Wei et al. showed that the edge sites and {100} faces of Pt nanoparticles have been fully covered by O atoms, while the O coverage on the terrace {111} is still below 0.5 ML[46]. The uncovered {111} terraces are then considered as the active face for ORR. The overall barrier of ORR on the terrace {111} is estimated to be 0.65 eV. To verify the influences of shape and size on the ORR activity, the mass activity (MA) is calculated by microkinetics. Two models (Model 1 and Model 2) are used: In Model 1, the shape of Pt nanoparticles varies according to the improved Wulff construction; while in Model 2, the shape is fixed at $D_{(100)}/D_{(111)} = 1$ for all sizes. Both models yield a maximum MA at $D_{(111)}$ of ~ 2 nm, suggesting that the ORR activity does not change monotonously with particle size, but has an optimal particle size.

4 Applications of SSW-NN in Electrochemical Simulations

The structure of active site in the above study was constructed manually based on experimental information. However, since it is usually difficult to determine the precise structure of the active site from experiments, the reliability of theoretical simulations, to some extent, depends on whether the constructed model is close to the real catalyst. Fang et al. recently applied the first theoretical attempt to elucidate the *in-situ* surface structures of the stepped Pt(110) at 0.0 V ~ 0.4 V from first principles. By using SSW-NN

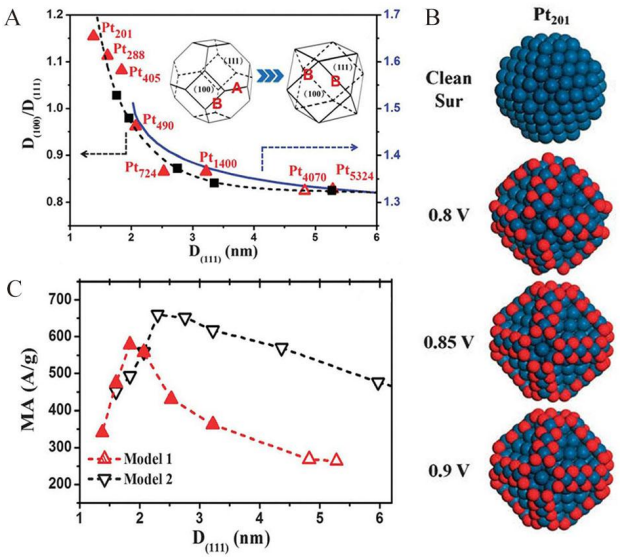

Figure 6. (A) The size vs. shape diagram for Pt nanoparticles from experiment (black) and theory (blue)[46]. (B) Calculated MA of Pt nanoparticles[46]. (C) Surface composition of Pt_{201} by combining thermodynamics and the steady-state kinetics analysis using DFT/CM-MPB calculations[46]. Blue balls: Pt; red balls: O. Reproduced with permission of Ref. 46(A-C). Copyright with 2013 Royal Society of Chemistry. (color on line)

global optimization, they discovered a (1 × 1) disordering at +0.20 V when the H coverage is above 0.60 ML. This reconstruction produces the key five-coordinated Pt sites that exhibit the superior activity for hydrogen evolution reaction (HER) and are the key species responsible for the high HER activity of Pt electrode[48]. Their results demonstrated that the SSW-NN method is a promising approach to track the complex electrochemical processes that couple structural evolution and surface reactions.

For ORR, we recently trained a global NN potential for the Pt-Ni-Mo-O-H pentad system, which allows us to carry out SSW-NN calculations on ORR catalysts such as PtNi and PtNiMo alloys. For example, we have explored the pathway and energetic profile for the structural evolution of $Pt_3Ni(111)$ at 0.9 V, and the results are shown in Figure 7. On the bare $Pt_3Ni(111)$ surface, the surface layer is Pt skin, while the subsurface layer is enriched with Ni atoms (see 0O state). This surface structure is well consistent with the previous theoretical and experimental results[49]. At 0.9 V, the bare $Pt_3Ni(111)$ would be notably oxidated due to the increase of O coverage. Specifically, below 0.08 ML O coverage, the Pt skin is maintained. As the O coverage increases up to 0.17 ML, the subsurface Ni atoms progressively substitute the surface Pt near the O adatoms to expose a Pt-Ni mixed surface. As for the higher O coverage, the surface reconstructs by forming a square-planar-coordinated NiO_2 chain that lifts from the surface (see the ball-and-stick moiety). The energetic profile shows that the most stable surface is the reconstructed surface covered by 0.75 ML O. Note that the exposed Ni can further be leached from the surface, making the structure much more complicated than we present here. Further works by using the state-of-the-art methods are required to reveal the exact surface structures for Pt_3Ni under ORR conditions.

5 Conclusions and Outlooks

In this work, we review the recent advances in the theoretical simulations of electrocatalysis based on the first-principles and ML methods. The details of double reference approach and CM-MPB that can describe the electric double layer are provided. Furthermore, the key features of SSW-NN method as an implemented in LASP software are elaborated, which can predict the structural evolution of electrode surface from the first principles. Using these new meth-

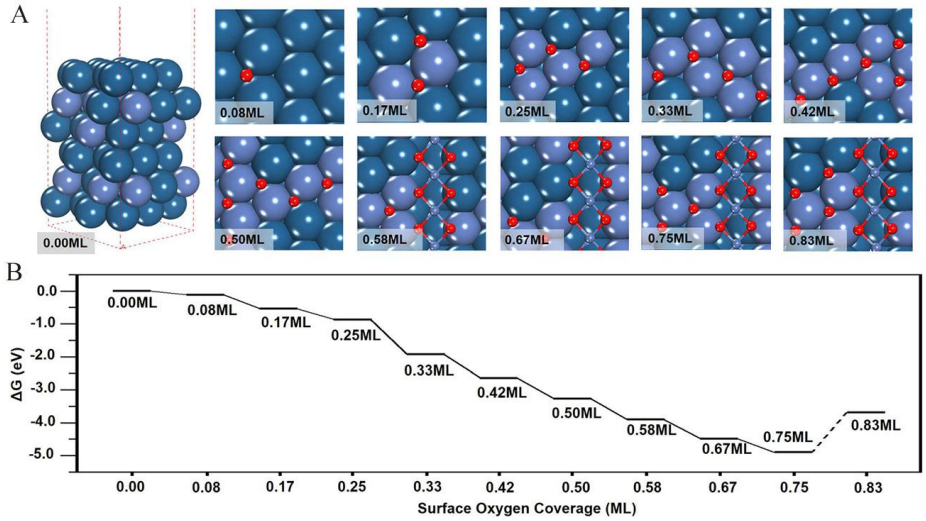

Figure 7. Structures and energetic profiles for the evolution of $Pt_3Ni(111)$ under ORR conditions at 0.9 V vs. RHE. (A) Atomic structures of intermediate states. The atoms above the (111) surface plane are depicted in the ball-and-stick style, while other atoms are depicted in the CPK style. (B) Energetic profiles for the evolution of $Pt_3Ni(111)$. Colors in (A): Blue balls are Pt; Violet balls are Ni; Red balls are O. (color on line)

ods, the Tafel kinetics of ORR, the corrosion mechanism, and the *in-situ* surface structures of Pt electrode are revealed.

While tremendous progress has been made in recent years, many more challenges for simulations of electrocatalysis are identified and need to be solved by theory in the future. For instance, the NN PES is not compatible with the charged slab model used in kinetics simulations. At present, the NN PES is trained at neutral conditions (without a net charge), without considering the influences of electric double layer and solvation. In the electrochemical process, the electrode surface is charged. To achieve the electrochemical properties, we need to train the NN PES at a charged condition. This approach, however, sacrifices the generality of the NN PES, that is, this NN PES can only be used to simulate the surface with a predefined surface charge density. How to generate a PES that can represent the surfaces under electrochemical conditions is still a challenge.

The most severe drawback of the constant electron number mode is the drift of electrode potential caused by dissimilar charge states of intermediate species. To ensure that the electrode potential is constant, a sufficiently large cell is required, which is, however, expensive in computational cost. The method based on the constant electron chemical po tential mode is still being developed, which may finally resolve this problem.

In photo-electrochemical catalysis on semiconductors, the charge is localized as polarons, which is notably different from the free electron in metal electrodes. The theoretical methods introduced in this article are developed based on the free-electron approximation. It is still unclear whether the concepts based on the development of metal electrochemical reactions, such as electric double layer and Tafel slope, are still valid in photo-electrochemical catalysis.

Acknowledgments:

This work was supported by the National Key Research and Development Program of China (2018YFA0208600), and the National Science Foundation of China (21773032, 21972023, 21533001, 22022301, 91545107, 91745201).

ORICID

Ye-Fei Li: 0000-0003-4433-7433

Zhi-Pan Liu: 0000-0002-2906-5217

References:

[1] Yang Z G, Zhang J L, Kintner-Meyer M C W, Lu X C,

Choi D, Lemmon J P, Liu J. Electrochemical energy storage for green grid[J]. Chem. Rev., 2011, 111(5): 3577-3613.

[2] Jukk K, Alexeyeva N, Ritslaid P, Kozlova J, Sammelselg V, Tammeveski K. Electrochemical reduction of oxygen on heat-treated Pd nanoparticle/multi-walled carbon nanotube composites in alkaline solution[J]. Electrocatalysis, 2013, 4(1): 42-48.

[3] Gasteiger H A, Markovic N M. Just a dream-or future reality [J]. Science, 2009, 324(5923): 48-49.

[4] Tian N, Zhou Z Y, Sun S G, Ding Y, Wang Z L. Synthesis of tetrahexahedral platinum nanocrystals with high-index facets and high electro-oxidation activity[J]. Science, 2007, 316(5825): 732-735.

[5] Stamenkovic V R, Mun B S, Mayrhofer K J J, Ross P N, Markovic N M. Effect of surface composition on electronic structure, stability, and electrocatalytic properties of Pt-transition metal alloys: Pt-skin versus Pt-skeleton surfaces[J]. J. Am. Chem. Soc., 2006, 128(27): 8813-8819.

[6] Gasteiger H A, Kocha S S, Sompalli B, Wagner F T. Activity benchmarks and requirements for Pt, Pt-alloy, and non-Pt oxygen reduction catalysts for PEMFCs[J]. Appl. Catal. B, 2005, 56(1): 9-35.

[7] Zhu J, Hu L, Zhao P, Lee L Y S, Wong K Y. Recent advances in electrocatalytic hydrogen evolution using nanoparticles[J]. Chem. Rev., 2020, 120(2): 851-918.

[8] Lim B, Jiang M J, Camargo P H C, Cho E C, Tao J, Lu X M, Zhu Y M, Xia Y N. Pd-Pt bimetallic nanodendrites with high activity for oxygen reduction[J]. Science, 2009, 324(5932): 1302-1305.

[9] Zhang J, Sasaki K, Sutter E, Adzic R R. Stabilization of platinum oxygen-reduction electrocatalysts using gold clusters[J]. Science, 2007, 315(5809): 220-222.

[10] Fang Y H, Liu Z P. Tafel kinetics of electrocatalytic reactions: from experiment to first-principles[J]. ACS Catal., 2014, 4(12): 4364-4376.

[11] Gouy M. Sur la constitution de la charge électrique à la surface d'un électrolyte[J]. J. Phys. Theor. Appl., 1910, 9 (1): 457-468.

[12] Chapman D L. LI. A contribution to the theory of electrocapillarity[J]. Philos. Mag., 1913, 25(148): 475-481.

[13] Stern O. Zur theorie der elektrolytischen doppelschicht [J]. Elektrochem. Angew. Phys. Chem., 1924, 30(21-22): 508-516.

[14] Furuya N, Shibata M. Structural changes at various Pt single crystal surfaces with potential cycles in acidic and alkaline solutions[J]. J. Electroanal. Chem., 1999, 467(1): 85-91.

[15] Basdogan Y, Maldonado A M, Keith J A. Advances and challenges in modeling solvated reaction mechanisms for renewable fuels and chemicals[J]. Wires Comput. Mol. Sci., 2020, 10(2): e1446.

[16] Wang H F, Liu Z P. Formic acid oxidation at Pt/H_2O interface from periodic DFT calculations integrated with a continuum solvation model[J]. J. Phys. Chem. C, 2009, 113 (40): 17502-17508.

[17] Li Y F, Liu Z P, Liu L, Gao W. Mechanism and activity of photocatalytic oxygen evolution on titania anatase in aqueous surroundings[J]. J. Am. Chem. Soc., 2010, 132(37): 13008-13015.

[18] Fang Y H, Liu Z P. Electrochemical reactions at the electrode/solution interface: theory and applications to water electrolysis and oxygen reduction[J]. Sci. China Chem., 2010, 53(3): 543-552.

[19] Shang C, Liu Z P. Stochastic surface walking method for structure prediction and pathway searching[J]. J. Chem. Theory Comput., 2013, 9(3): 1838-1845.

[20] Shang C, Liu Z P. Constrained broyden minimization combined with the dimer method for locating transition state of complex reactions[J]. J. Chem. Theory Comput., 2010, 6(4): 1136-1144.

[21] Artrith N, Urban A, Ceder G. Constructing first-principles phase diagrams of amorphous Li_xSi using machine-learning-assisted sampling with an evolutionary algorithm[J]. J. Chem. Phys., 2018, 148(24): 241711.

[22] Wales D J, Doye J P K. Global optimization by basin-hopping and the lowest energy structures of lennard-Jones clusters containing up to 110 atoms[J]. J. Phys. Chem. A, 1997, 101(28): 5111-5116.

[23] Hart G L W, Mueller T, Toher C, Curtarolo S. Machine learning for alloys[J]. Nat. Rev. Mater., 2021, 6(8): 730-755.

[24] Norskov J K, Rossmeisl J, Logadottir A, Lindqvist L, Kitchin J R, Bligaard T, Jonsson H. Origin of the overpotential for oxygen reduction at a fuel-cell cathode[J]. J. Phys. Chem. B, 2004, 108(46): 17886-17892.

[25] Lozovoi A Y, Alavi A, Kohanoff J, Lynden-Bell R M. Ab initio simulation of charged slabs at constant chemical potential[J]. J. Chem. Phys., 2001, 115(4): 1661-1669.

[26] Nörskov J K, Bligaard T, Rossmeisl J, Christensen C H. Towards the computational design of solid catalysts[J]. Nat. Chem., 2009, 1(1): 37-46.

[27] Filhol J S, Neurock M. Elucidation of the electrochemical activation of water over Pd by first principles[J]. Angew. Chem. Int. Ed., 2006, 45(3): 402-406.

[28] Reiss H, Heller A. The absolute potential of the standard

hydrogen electrode: a new estimate[J]. J. Phys. Chem, 1985, 89(20): 4207-4213.

[29] Janik M J, Taylor C D, Neurock M. First principles analysis of the electrocatalytic oxidation of methanol and carbon monoxide[J]. Top. Catal., 2007, 46(3): 306-319.

[30] Fattebert J L, Gygi F. Density functional theory for efficient ab initio molecular dynamics simulations in solution[J]. J. Comput. Chem., 2002, 23(6): 662-666.

[31] Fattebert J L, Gygi F. Linear-scaling first-principles molecular dynamics with plane-waves accuracy[J]. Phys. Rev. B, 2006, 73(11): 115124.

[32] Fang Y H, Liu Z P. Surface phase diagram and oxygen coupling kinetics on flat and stepped Pt surfaces under electrochemical potentials[J]. J. Phys. Chem. C, 2009, 113 (22): 9765-9772.

[33] Fang Y H, Wei G F, Liu Z P. Theoretical modeling of electrode/electrolyte interface from first-principles periodic continuum solvation method[J]. Catal. Today, 2013, 202: 98-104.

[34] Shang C, Zhang X J, Liu Z P. Stochastic surface walking method for crystal structure and phase transition pathway prediction[J]. Phys. Chem. Chem. Phys., 2014, 16(33): 17845-17856.

[35] Wei G F, Liu Z P. Restructuring and hydrogen evolution on Pt nanoparticle[J]. Chem. Sci., 2015, 6(2): 1485-1490.

[36] Li Y F, Liu Z P. Particle size, shape and activity for photocatalysis on titania anatase nanoparticles in aqueous surroundings[J]. J. Am. Chem. Soc., 2011, 133(39): 15743-15752.

[37] Zhang X J, Shang C, Liu Z P. Stochastic surface walking reaction sampling for resolving heterogeneous catalytic reaction network: A revisit to the mechanism of water-gas shift reaction on Cu[J]. J. Chem. Phys., 2017, 147 (15): 152706.

[38] Behler J. First principles neural network potentials for reactive simulations of large molecular and condensed systems[J]. Angew. Chem. Int. Ed., 2017, 56(42): 12828-12840.

[39] Huang S D, Shang C, Zhang X J, Liu Z P. Material discovery by combining stochastic surface walking global optimization with a neural network[J]. Chem. Sci., 2017, 8(9): 6327-6337.

[40] Huang S D, Shang C, Kang P L, Zhang X J, Liu Z P. LASP: Fast global potential energy surface exploration [J]. Wires. Comput. Mol. Sci., 2019, 9(6): e1415.

[41] Hansen H A, Rossmeisl J, Nörskov J K. Surface pourbaix diagrams and oxygen reduction activity of Pt, Ag and Ni (111) surfaces studied by DFT[J]. Phys. Chem. Chem. Phys., 2008, 10(25): 3722-3730.

[42] Wei G F, Fang Y H, Liu Z P. First principles tafel kinetics for resolving key parameters in optimizing oxygen electrocatalytic reduction catalyst[J]. J. Phys. Chem. C, 2012, 116(23): 12696-12705.

[43] He Q G, Yang X F, Chen W, Mukerjee S, Koel B, Chen S W. Influence of phosphate anion adsorption on the kinetics of oxygen electroreduction on low index Pt (hkl) single crystals[J]. Phys. Chem. Chem. Phys., 2010, 12(39): 12544-12555.

[44] Fang Y H, Liu Z P. Toward anticorrosion electrodes: site-selectivity and self-acceleration in the electrochemical corrosion of platinum[J]. J. Phys. Chem. C, 2010, 114 (9): 4057-4062.

[45] Wei G F, Liu Z P. Towards active and stable oxygen reduction cathodes: a density functional theory survey on Pt_2M skin alloys[J]. Energy Environ. Sci., 2011, 4(4): 1268-1272.

[46] Wei G F, Liu Z P. Optimum nanoparticles for electrocatalytic oxygen reduction: the size, shape and new design[J]. Phys. Chem. Chem. Phys., 2013, 15(42): 18555-18561.

[47] Leontyev I N, Belenov S V, Guterman V E, Haghi-Ashtiani P, Shaganov A P, Dkhil B. Catalytic activity of carbon-supported Pt nanoelectrocatalysts. Why reducing the size of Pt nanoparticles is not always beneficial[J]. J. Phys. Chem. C, 2011, 115(13): 5429-5434.

[48] Fang Y H, Song D D, Li H X, Liu Z P. Structure and activity of potential-dependent Pt(110) surface phases revealed from machine-learning atomic simulation[J]. J. Phys. Chem. C, 2021, 125(20): 10955-10963.

[49] Stamenkovic V R, Fowler B, Mun B S, Wang G, Ross P N, Lucas C A, Markovic N M. Improved oxygen reduction activity on $Pt_3Ni(111)$ via increased surface site availability[J]. Science, 2007, 315(5811): 493-497.

电化学理论模拟方法的发展及其在铂基燃料电池中的应用

李吉利[1],李晔飞[1*],刘智攀[1,2*]

(1. 复旦大学化学系,能源材料化学协同创新中心(教育部),上海市分子催化和功能材料重点实验室,上海 200433; 2. 中国科学院上海有机化学研究所,有机功能分子合成与组装化学重点实验室,上海有机功能分子研究所,上海 200032)

摘要: 电化学中的理论计算模拟对于从原子水平理解电化学过程中的机制至关重要，它可以弥补许多实验上无法解释的现象,如果能在原子尺度上确定理解反应的活性中心,得到电极或电催化剂结构的演变过程,建立反应的微观机理,从根本上解决电极氧化和腐蚀的问题,提高电化学催化剂的活性和稳定性,从而设计更高效的电催化剂。然而,电化学的理论计算模拟中仍然存在诸多问题,例如,溶剂化效应的实现、电极/电解质(金属/溶液)界面之间合适的模拟模型和方法、电化学过程中的结构演化以及如何降低结构计算的计算代价等。在这里,我们回顾了电化学建模方法的最新进展以及我们小组通过使用修正的泊松-玻尔兹曼连续介质溶剂化模型模拟溶剂化效应对溶剂化效应和模型进行改进。同时为了减少计算代价,我们更关注机器学习在电化学模拟中的应用,主要分为两个部分,即通过快速对多种不同组分的能量进行计算并筛选出合适组分,但是无法得到实际的结构演变情况。另一个是通过快速结构取样得到不同组分不同的结构变化能够更为直观的获得结构的演变过程,从而揭示反应的机理。我们以本课题组开发的 SSW-NN 的方法为例,总结了基于机器学习的原子模拟在电化学方面的应用,介绍了 SSW-NN,模拟电化学反应条件下电极和电催化剂的氧化和腐蚀,并阐明了催化剂结构的活性和稳定性。

关键词: 连续介质化溶剂模型;机器学习;SSW-NN;LASP